Explicit Navier-Stokes Computation of Cascade Flows Using the k-ϵ Turbulence Model

Robert F. Kunz* and Budugur Lakshminarayana†
Pennsylvania State University, University Park, Pennsylvania 16802

A fully explicit two-dimensional flow solver, based on a four-stage Runge-Kutta scheme, has been developed and used to predict two-dimensional viscous flow through turbomachinery cascades for which experimental data are available. The formulation is applied to the density-weighted time-averaged Navier-Stokes equations. Several features of the technique improve the ability of the code to predict high Reynolds number flows on highly stretched grids. These include a low Reynolds number compressible form of the k-ϵ turbulence model, anisotropic scaling of artificial dissipation terms, and locally varying timestep evaluation based on hyperbolic and parabolic stability considerations. Comparisons between computation and experiment are presented for both a supersonic and a low-subsonic compressor cascade. These results indicate that the code is capable of predicting steady two-dimensional viscous cascade flows over a wide range of Mach numbers in reasonable computation times.

Nomenclature

a	= speed of sound
C_p	= pressure coefficient, $(p - p_\infty)/\frac{1}{2}\rho_\infty V_m^2$
c	= chord length
c_p, c_v	= specific heat at constant pressure and volume
$\boldsymbol{E}$, $\boldsymbol{F}$	= flux vectors
e	= internal energy per unit mass
e_0	= total energy per unit mass, $(e + V^2/2)$
G_1, G_2	= contravariant velocity components
J	= Jacobian of curvilinear transformation
k	= turbulent kinetic energy
L	= turbulence length scale
n, s	= blade normal and chordwise coordinates
P	= production term in turbulent kinetic energy equation
Pr_l,Pr_t,Pr_k,Pr_ϵ	= Prandtl numbers
p	= static pressure
$\boldsymbol{Q}$	= primary transport variable vector
q_i	= Cartesian components of heat transfer rate vector
$\boldsymbol{R}$	= residual vector
$\boldsymbol{S}$	= source term vector
T	= static temperature
T_u	= turbulence intensity
t	= pitch length
u,v	= Cartesian velocity components
V	= magnitude of total velocity
x,y	= Cartesian coordinates
α	= exponent in artificial dissipation scaling function
β_1,β_2	= incidence and deviation angles
δ_{ij}	= Kronecker delta
$\delta_{\xi\xi}$, $\delta_{\eta\eta}$, $\delta_{\xi\xi\xi\xi}$, $\delta_{\eta\eta\eta\eta}$	= central differencing operators
γ	= specific heat ratio
Δt	= local timestep
ϵ	= isotropic turbulent kinetic energy dissipation rate
κ_2, κ_4	= artificial dissipation constants
μ_1, μ_t	= molecular and turbulent viscosities
ν_{ij}	= pressure monitoring parameter for artificial dissipation
ξ, η	= curvilinear coordinates
ρ	= density
σ_2, σ_4	= artificial dissipation weighting function
τ_{ij}	= Cartesian components of stress tensor

Subscripts

c	= convective
i, j	= grid indices in streamwise and pitchwise directions, respectively
l	= laminar
m	= cascade mean value (average of inlet and outlet quantities)
max	= maximum local (boundary-layer edge) value
ps	= pressure surface
sep	= separation point
ss	= suction surface
t	= turbulent
v	= viscous
w	= wall
θ	= cascade pitchwise direction
∞	= inlet freestream
0	= stagnation
2	= cascade outlet condition

Superscripts

$\hat{}$	= quantity scaled by metric Jacobian
$'$	= fluctuating quantity in time averaging
$''$	= fluctuating quantity in density-weighted time averaging
$\bar{}$	= time-averaged quantity
$\tilde{}$	= density-weighted time-averaged quantity

Received April 9, 1990; revision received Sept. 28, 1990; accepted for publication Oct. 5, 1990.

*Graduate Student, Department of Aerospace Engineering; currently Consultant, General Motors Technical Center, C1-TRANS, Warren, MI 48090. Member AIAA.

†Evan Pugh Professor of Aerospace Engineering, Department of Aerospace Engineering. Fellow AIAA.

Introduction

COMPUTATION of viscous flows by numerically solving the Navier-Stokes equations has become increasingly feasible due for the most part to the ever increasing speed and memory of digital computers. State of the art computational fluid dynamics codes available today are capable of calculating steady three-dimensional viscous flows about entire vehicles, and even unsteady viscous flows in three-dimensional

turbomachinery stages. However, despite the rapid advance toward exploiting the power of the computers now available, some serious limitations of these codes have yet to be adequately resolved. Surely the most profound of these is the lack of accurate and general turbulence models. Secondary to this, but of much concern, is the role of artificial dissipation in Navier-Stokes calculations.

Explicit schemes, such as the Runge-Kutta methods first applied to the solution of the Euler equations by Jameson et al.[1] offer several appealing characteristics in application to fluid flow computations. Such schemes are easily vectorizable, amenable to convergence acceleration techniques, and can be extended to unsteady flow computations in a straightforward manner. However, because of the stiffness associated with explicit treatment of transport equations containing large source terms, incorporation of higher order turbulence models, which contain such source terms, has not been popular in explicit flow solvers.

Often, algebraic eddy viscosity models are used to approximate the apparent stresses in explicit codes. These models have little computational overhead, and do not adversely affect the stability of the scheme. Though very useful in computing attached or slightly separated boundary-layer flows, such models have well-recognized drawbacks in the computation of complex flows where multiple length scales exist and where the transport of turbulent length scales is important. Though the k-ϵ turbulence model also has major deficiencies (e.g., Speziale[2] and Lakshminarayana[3]), it does provide the transport of length scale, which is computed based on local fluid and turbulence properties. The model has been shown by Kirtley and Lakshminarayana[4] to provide better predictions than algebraic models for two-dimensional flow with adverse pressure gradient, and by Degrez and VanDromme[5] for two-dimensional shock boundary-layer flow on curved surfaces. It therefore seemed worthwhile to try to use it to provide an improved engineering approximation to the complex cascade flowfields investigated herein.

Implicit flow solvers have been used for well over a decade to compute compressible turbulent flows using various forms of the k-ϵ turbulence model. However, there have been only a few attempts to incorporate the model into an explicit solution procedure. In these cases, the stiffness problems associated with explicit treatment of the k-ϵ model have been circumvented by incorporating semi-implicit treatment of the source terms,[6] by implementation of an algebraic inner layer model coupled to a high Reynolds number form of the k-ϵ model in the outer layer,[6] or by using wall functions to model, rather than to resolve, the near-wall region where source terms and grid aspect ratio can be large.[7-9]

The use of higher order turbulence models, and the precise control of levels of artificial dissipation, can improve the accuracy of high Reynolds number flow computations about complex configurations. The main thrusts of this investigation are the incorporation of a low Reynolds number compressible form of the k-ϵ turbulence model into a purely explicit scheme, and the application of the technique to flows across a wide range of Mach numbers. In addition, some recent improvements in controlling artificial dissipation levels in the computation of viscous flows on highly stretched grids are tested and incorporated. Two complex cascade flows are computed, for supersonic and low subsonic freestream conditions. For the supersonic cascade, isentropic blade Mach number, shock boundary-layer structure, and wake loss profiles are compared with experimentally measured values. Pressure distribution and boundary-layer profiles of velocity and turbulent kinetic energy are compared with data for the subsonic cascade. The results are shown to be quite good, within the accuracy of the turbulence model and experimental data used.

Governing Equations and Turbulence Model

In the present development, the density-weighted time-averaging attributed to Favre[10] is used. This decomposition has advantages in flow computations with variable density (see Jones[11]). Specifically, the averaged governing equations are of simpler form and the physical interpretation of terms in the equations is clearer than when conventional time averaging is used. Reynolds (time) averaging, defined for a scalar ϕ as

$$\phi = \bar{\phi} + \phi'$$

where

$$\bar{\phi} = \lim_{T\to\infty} \frac{1}{T} \int_{t_0}^{t_0+T} \phi \, dt \tag{1}$$

is used for pressure, density, molecular stress tensor, and molecular heat flux vector. Favre (density-weighted time) averaging, defined for scalar ϕ as

$$\phi = \tilde{\phi} + \phi''$$

where

$$\tilde{\phi} = \overline{\rho\phi}/\bar{\rho} \tag{2}$$

is used for velocity components, internal energy, turbulent kinetic energy, and turbulent energy dissipation rate. The resulting Favre-averaged two-dimensional Navier-Stokes equations can be written in conservative form in generalized body fitted coordinates as

$$\frac{\partial \hat{Q}}{\partial t} + \left(\frac{\partial \hat{E}_c}{\partial \xi} + \frac{\partial \hat{F}_c}{\partial \eta}\right) = \left(\frac{\partial \hat{E}_v}{\partial \xi} + \frac{\partial \hat{F}_v}{\partial \eta}\right) + \hat{S} \tag{3}$$

where

$$\hat{Q} = \frac{1}{J}\begin{bmatrix} \bar{\rho} \\ \bar{\rho}\tilde{u} \\ \bar{\rho}\tilde{v} \\ \bar{\rho}\tilde{e}_0 \end{bmatrix}, \qquad \hat{E}_c = \frac{1}{J}\begin{bmatrix} \bar{\rho}\tilde{G}_1 \\ \bar{\rho}\tilde{u}\tilde{G}_1 + \xi_x\bar{p} \\ \bar{\rho}\tilde{v}\tilde{G}_1 + \xi_y\bar{p} \\ (\bar{\rho}\tilde{e}_0 + \bar{p})\tilde{G}_1 \end{bmatrix}$$

$$\hat{F}_c = \frac{1}{J}\begin{bmatrix} \bar{\rho}\tilde{G}_2 \\ \bar{\rho}\tilde{u}\tilde{G}_2 + \eta_x\bar{p} \\ \bar{\rho}\tilde{v}\tilde{G}_2 + \eta_y\bar{p} \\ (\bar{\rho}\tilde{e}_0 + \bar{p})\tilde{G}_2 \end{bmatrix}$$

$$\hat{E}_v = \frac{1}{J}\begin{bmatrix} 0 \\ \xi_x\tau_{xx} + \xi_y\tau_{yx} \\ \xi_x\tau_{xy} + \xi_y\tau_{yy} \\ \xi_x(\tilde{u}\tau_{xx} + \tilde{v}\tau_{xy} - q_x) + \xi_y(\tilde{u}\tau_{yx} + \tilde{v}\tau_{yy} - q_y) \end{bmatrix}$$

$$\hat{F}_v = \frac{1}{J}\begin{bmatrix} 0 \\ \eta_x\tau_{xx} + \eta_y\tau_{yx} \\ \eta_x\tau_{xy} + \eta_y\tau_{yy} \\ \eta_x(\tilde{u}\tau_{xx} + \tilde{v}\tau_{xy} - q_x) + \eta_y(\tilde{u}\tau_{yx} + \tilde{v}\tau_{yy} - q_y) \end{bmatrix} \tag{4}$$

$$\hat{S} = \begin{bmatrix} 0 \\ 0 \\ 0 \\ 0 \end{bmatrix}$$

The metric terms and contravariant velocity components are given by

$$\xi_x = \frac{\partial \xi}{\partial x}, \qquad \xi_y = \frac{\partial \xi}{\partial y}, \qquad \eta_x = \frac{\partial \eta}{\partial x}, \qquad \eta_y = \frac{\partial \eta}{\partial y} \tag{5}$$

$$J = \xi_x\eta_y - \eta_x\xi_y$$

$$\tilde{G}_1 = \xi_x\tilde{u} + \xi_y\tilde{v}, \qquad \tilde{G}_2 = \eta_x\tilde{u} + \eta_y\tilde{v} \tag{6}$$

A perfect gas equation of state is given as $\bar{p} = \bar{\rho} R \tilde{T}$, where

$$\tilde{T} = \frac{1}{c_v}\left(\tilde{e}_0 - \frac{\tilde{V}^2}{2}\right)$$

Incorporating an eddy viscosity formulation, the effective stress tensor and the effective heat flux vector are given in Cartesian coordinates by

$$\tau_{ij} = \tau_{lij} - \overline{\rho u_i'' u_j''}$$

$$= (\mu_l + \mu_t)\left[\left(\frac{\partial \tilde{u}_i}{\partial x_j} + \frac{\partial \tilde{u}_j}{\partial x_i}\right) - \frac{2}{3}\delta_{ij}\frac{\partial \tilde{u}_k}{\partial x_k}\right] - \frac{2}{3}\delta_{ij}\bar{\rho}\tilde{k}$$

$$q_i = -\tilde{k}\frac{\partial \tilde{T}}{\partial x_i} + \overline{\rho u_i'' e''} = -c_p\left(\frac{\mu_l}{Pr_l} + \frac{\mu_t}{Pr_t}\right)\frac{\partial \tilde{T}}{\partial x_i} \tag{7}$$

In the present work, the Favre-averaged k-ϵ equations are numerically decoupled from the Favre-averaged mean flow equations. Specifically, at each iteration, the four mean flow equations are updated using "frozen" values of eddy viscosity and turbulent kinetic energy from the previous iteration. Likewise, the coupled k-ϵ equations are then updated using the "frozen" mean flow quantities just computed.

Low Reynolds number forms of the compressible k-ϵ equations can be written in the same form as Eq. (3), where the scaled variable vectors become

$$\hat{Q} = \frac{1}{J}\begin{bmatrix}\bar{\rho}\tilde{k}\\ \bar{\rho}\tilde{\epsilon}\end{bmatrix}, \qquad \hat{E}_c = \frac{1}{J}\begin{bmatrix}\bar{\rho}\tilde{k}\tilde{G}_1\\ \bar{\rho}\tilde{\epsilon}\tilde{G}_1\end{bmatrix}, \qquad \hat{F}_c = \frac{1}{J}\begin{bmatrix}\bar{\rho}\tilde{k}\tilde{G}_2\\ \bar{\rho}\tilde{\epsilon}\tilde{G}_2\end{bmatrix}$$

$$\hat{E}_v = \frac{1}{J}\begin{Bmatrix}\left[\mu_1 + \frac{\mu_t}{Pr_k}\right] & \left[(\nabla\xi\cdot\nabla\xi)\frac{\partial \tilde{k}}{\partial \xi} + (\nabla\xi\cdot\nabla\eta)\frac{\partial \tilde{k}}{\partial \eta}\right]\\ \left[\mu_1 + \frac{\mu_t}{Pr_\epsilon}\right] & \left[(\nabla\xi\cdot\nabla\xi)\frac{\partial \tilde{\epsilon}}{\partial \xi} + (\nabla\xi\cdot\nabla\eta)\frac{\partial \tilde{\epsilon}}{\partial \eta}\right]\end{Bmatrix}$$

$$\hat{F}_v = \frac{1}{J}\begin{Bmatrix}\left[\mu_1 + \frac{\mu_t}{Pr_k}\right] & \left[(\nabla\eta\cdot\nabla\xi)\frac{\partial \tilde{k}}{\partial \xi} + (\nabla\eta\cdot\nabla\eta)\frac{\partial \tilde{k}}{\partial \eta}\right]\\ \left[\mu_1 + \frac{\mu_t}{Pr_\epsilon}\right] & \left[(\nabla\eta\cdot\nabla\xi)\frac{\partial \tilde{\epsilon}}{\partial \xi} + (\nabla\eta\cdot\nabla\eta)\frac{\partial \tilde{\epsilon}}{\partial \eta}\right]\end{Bmatrix}$$

$$\hat{S} = \frac{1}{J}\begin{bmatrix}P - \bar{\rho}\tilde{\epsilon} + \mathfrak{D}\\ (C_1 f_1 P - C_2 f_2 \bar{\rho}\tilde{\epsilon})\frac{\tilde{\epsilon}}{\tilde{k}} + \mathcal{E}\end{bmatrix} \tag{8}$$

where the production term P is given in Cartesian coordinates as

$$P = \left\{2\mu_t\frac{\partial \tilde{u}}{\partial x} - \frac{2}{3}\left[\bar{\rho}\tilde{k} + \mu_t\left(\frac{\partial \tilde{u}}{\partial x} + \frac{\partial \tilde{v}}{\partial y}\right)\right]\right\}\frac{\partial \tilde{u}}{\partial x}$$

$$+ \left\{2\mu_t\frac{\partial \tilde{v}}{\partial y} - \frac{2}{3}\left[\bar{\rho}\tilde{k} + \mu_t\left(\frac{\partial \tilde{u}}{\partial x} + \frac{\partial \tilde{v}}{\partial y}\right)\right]\right\}\frac{\partial \tilde{v}}{\partial y}$$

$$+ \mu_t\left(\frac{\partial \tilde{u}}{\partial y} + \frac{\partial \tilde{v}}{\partial x}\right)^2 \tag{9}$$

The mass-average turbulent kinetic energy and homogeneous component of turbulent kinetic energy dissipation rate are defined as

$$\tilde{k} = \frac{\frac{1}{2}\overline{\rho u_i'' u_i''}}{\bar{\rho}}, \qquad \tilde{\epsilon} = \frac{\overline{\nu\rho(\partial u_i''/\partial x_j)(\partial u_i''/\partial x_j)}}{\bar{\rho}} \tag{10}$$

The eddy viscosity is obtained from the Prandtl-Kolmogorov relation

$$\mu_t = \frac{C_\mu f_\mu \bar{\rho}\tilde{k}^2}{\tilde{\epsilon}} \tag{11}$$

The particular form of low Reynolds number model used in the code was originally devised by Chien for incompressible flow.[12] Compressible forms have been given by Coakley[13] and others. For this model, the constants and functions in Eqs. (8–11) are given by

$$f_\mu = 1 - \exp(-0.115y^+)$$

$$f_1 = 1, \qquad f_2 = 1 - (2/9)\exp(-R_T^2/36)$$

$$R_T = \bar{\rho}\tilde{k}^2/\mu_l\tilde{\epsilon}, \qquad y^+ = \bar{\rho}nu^*/\mu_l, \qquad u^* = \sqrt{\tau_w/\bar{\rho}}$$

$$\mathfrak{D} = -(2\mu_l\tilde{k}/n^2), \qquad \mathcal{E} = -(2\mu_l\tilde{\epsilon}/n^2)\exp(-0.5y^+) \tag{12}$$

where $C_\mu = 0.09$, $C_1 = 1.35$, $C_2 = 1.80$, $Pr_k = 1.0$, and $Pr_\epsilon = 1.3$. Following Hobson,[14] the blade normal coordinate n in Eq. (12) is replaced by absolute distance from leading and trailing edge, upstream and downstream of the passage, respectively.

The transport variable ϵ used in this model is the isotropic component of the dissipation rate, though the ϵ equation is derived for the homogeneous component of the dissipation rate. Near a solid wall the anisotropic dissipation component is not negligible, and the isotropic component ϵ goes to zero. The term $\mathfrak{D}$ accounts for the nonzero value of total dissipation near the wall, so that the model also remains valid near solid walls and retains the convenience of specifying the $\epsilon = 0$ boundary condition there.

It should be noted that, although the k-ϵ equations have been cast in compressible form, the modeling assumptions invoked here are essentially those for incompressible flow. Specifically, terms in the unmodeled k and ϵ equations containing density fluctuation terms ρ' are neglected. Also, pressure diffusion terms are neglected. No thin layer approximations are made in either the mean flow or turbulence transport equations.

Numerical Solution

Discretization

The H-grid flow solver used in the present studies incorporates a standard four-stage Runge-Kutta scheme, as first applied to Euler calculations by Jameson et al.[1] Here

$$\hat{Q}^1 = \hat{Q}^n + \tfrac{1}{4}\Delta t\hat{R}(\hat{Q}^n)$$

$$\hat{Q}^2 = \hat{Q}^n + \tfrac{1}{3}\Delta t\hat{R}(\hat{Q}^1)$$

$$\hat{Q}^3 = \hat{Q}^n + \tfrac{1}{2}\Delta t\hat{R}(\hat{Q}^2)$$

$$\hat{Q}^{n+1} = \hat{Q}^n + \Delta t\hat{R}(\hat{Q}^3) \tag{13}$$

and the residual $\hat{R}$ is defined according to

$$\hat{R} = -\left(\frac{\partial \hat{E}_c}{\partial \xi} + \frac{\partial \hat{F}_c}{\partial \eta}\right) + \left(\frac{\partial \hat{E}_v}{\partial \xi} + \frac{\partial \hat{F}_v}{\partial \eta}\right) + \hat{S} \tag{14}$$

Second-order accurate central differences are used to discretize the spatial derivatives in Eq. (14). Viscous and source terms are evaluated prior to the first stage, convective terms are computed at every stage. The scheme is first-order accurate in time.

To accelerate the solution to steady state, locally varying timesteps are computed based on a linear stability analysis of

the discretized Navier-Stokes equations. The resulting time-step specification is given as

$$\Delta t = \min[\Delta t_c, \Delta t_v] = \min\left[\frac{\text{IMAG}}{|\tilde{G}_1| + a\sqrt{\nabla\xi\cdot\nabla\xi}) + |\tilde{G}_2| + a\sqrt{(\nabla\eta\cdot\nabla\eta)}}\right.$$
$$\left.\frac{\text{REAL}}{\frac{4\gamma}{\tilde{\rho}}\left(\frac{\mu_1}{Pr_l}+\frac{\mu_t}{Pr_t}\right)[(\nabla\xi\cdot\nabla\xi)+(\nabla\eta\cdot\nabla\eta)]+\frac{1}{3\tilde{\rho}}(\mu_1+\mu_t)[7|\nabla\xi\cdot\nabla\eta|+\sqrt{(\nabla\xi\cdot\nabla\xi)(\nabla\eta\cdot\nabla\eta)}]}\right] \tag{15}$$

Here, IMAG and REAL are input parameters corresponding to operational Courant-Friedrichs-Lewy (CFL) and Von Neumann numbers chosen to ensure stability. A similar expression is given by Martinelli.[15] The first term in the brackets in Eq. (15) arises from the convection operators, the latter term corresponds to physical viscous terms. Note that for the present uncoupled approach, the turbulent kinetic energy does not appear in the stability expressions.

The code uses body conforming H-grids. This simplifies application to new cases, implementation of boundary conditions and pre- and postprocessing, at the expense of grid orthogonality and resolution in the leading edge region. For large Reynolds number flows, the H-grids used must be highly stretched in the pitchwise direction, in order to adequately resolve near-wall gradients. Consequently, the metric terms η_x, η_y in Eq. (15) can become very large near the $j = 1$ and $j = nj$ boundaries. Also, when using a two-equation turbulence model, as in the present study, the eddy viscosity μ_t can be signifcantly larger than the molecular viscosity near the $j = 1$ and $j = nj$ boundaries, upstream and downstream of the blades, where wall damping effects are negligible. This combination of large eddy viscosity and grid metrics causes the viscous stability term to dominate in these regions, and it has been found that it is crucial to include the influence of these terms in determining a stable local timestep. For the supersonic and subsonic cascade test cases computed herein, $\Delta t_v < \Delta t_c$ for 40.0 and 7.5% of the grid points at convergence, respectively. Since local stability must be satisfied everywhere in the domain, the authors feel that the abovementioned considerations will be important in all explicit computations where the grid is clustered in regions away from the body surface, including C-grid and unstructured flow adaptive meshes. Even on H-grids, where η direction clustering is flared away from the $j = 1$ and $j = nj$ boundaries up- and downstream of the blade, it is unlikely that large η direction clustering can be adequately relaxed within the region of wall damping effects to completely avoid the local viscous stability constrants discussed.

Even for the computation of steady, one-dimensional, inviscid flows, the use of highly stretched grids gives rise to significantly reduced convergence rates in explicit schemes. This effect arises due to characteristic propagation speed in the streamwise direction. In two dimensions an analogous situation arises when the computational mesh is clustered in one curvilinear coordinate direction to resolve regions where flowfield gradients are large. Specifically, the maximum local stable timestep in regions where the mesh is highly clustered in the η direction is inversely proportional to the metric term $\sqrt{(\nabla\eta\cdot\nabla\eta)}$, which can be very large. It is the nature of this inviscid effect that often allows one to use a local timestep based solely on inviscid considerations, for viscous flow computations.

The k and ϵ equations each contain nonlinear production and destruction source terms, which can be very large near solid boundaries. According to linear stability theory, such terms can also severely reduce convergence rates if a purely explicit scheme is used to discretize the equations. It was found that by incorporating a composite viscous-inviscid timestep specification, the stability restrictions on the k-ϵ solution are not much more severe than the restrictions on the mean flow equations discussed above. In fact, it was possible to compute high Reynolds number flows with this turbulence model, using a purely explicit treatment in reasonable computation times. A local timestep for the k-ϵ equations of approximately one-fourth of the stable mean flow timestep was satisfactory for the cascade flows computed herein. Converged solutions were thereby obtained in computation times approximately twice those of solutions using an algebraic eddy viscosity model. This is illustrated for turbulent flat plate flow computations presented below.

Artificial Dissipation

In the present work, artificial dissipation is added to the discretized mean flow equations as

$$\hat{R} = -\left(\frac{\partial\hat{E}_c}{\partial\xi}+\frac{\partial\hat{F}_c}{\partial\eta}\right)+\left(\frac{\partial\hat{E}_v}{\partial\xi}+\frac{\partial\hat{F}_v}{\partial\eta}\right)+D(Q)+\hat{S} \tag{16}$$

Here, $D(Q)$ represents a mixed second- and fourth-difference nonconservative artificial dissipation operator, similar to that devised by Jameson et al.[1]

$$D(Q) = D_\xi(Q) + D_\eta(Q)$$
$$D_\xi(Q) = S_{2\xi}\delta_{\xi\xi}Q + S_{4\xi}\delta_{\xi\xi\xi\xi}Q$$
$$D_\eta(Q) = S_{2\eta}\delta_{\eta\eta}Q + S_{4\eta}\delta_{\eta\eta\eta\eta}Q \tag{17}$$

The fourth-difference operators are included to damp high wave number errors, and the second-difference operators are included to improve shock capturing.

As pointed out by Pulliam,[16] artificial dissipation terms should operate on physical values of the flowfield variables, so as to avoid unnecessary smoothing in regions where the grid is highly clustered, but gradients in the physical transport variables are small. For this reason, artificial dissipation operators must be appropriately scaled by the metric Jacobian. In addition to the preceding consistency requirement on the dissipation scaling, levels of dissipation should always be reduced to levels adequate to stabilize a scheme without altering the accuracy of the solution. For the computation of viscous flows on highly stretched grids, this latter requirement is a sensitive matter.

For high Reynolds number flows, very highly stretched grids must be used to resolve body normal gradients in near-wall regions. If the artificial dissipation terms in both the ξ and η directions are scaled by the local timestep, on grids which are highly stretched in the η direction, excessive dissipation is introduced in the ξ direction. (This effect is discussed by Caughey and Turkel[17] and Swanson and Turkel.[18]) This excessive dissipation may reduce accuracy and convergence rates in viscous flow computations. A recently devised eigenvalue scaling of the artificial dissipation terms, due to Martinelli,[15] alleviates this problem. Since the present technique is primarily used to compute viscous flows on highly stretched grids, anisotropic dissipation scaling factors similar to those used by Martinelli are incorporated. In Eqs. (17) $S_{2\xi}$, $S_{2\eta}$, $S_{4\xi}$, $S_{4\eta}$ are defined by

$$S_{2\xi} = \frac{\sigma_{2\xi}}{J}\left[\frac{1}{\Delta t_{c\xi}}\left(1+\frac{\Delta t_{c\xi}}{\Delta t_{c\eta}}\right)^\alpha\right], \quad S_{2\eta} = \frac{\sigma_{2\eta}}{J}\left[\frac{1}{\Delta t_{c\eta}}\left(1+\frac{\Delta t_{c\eta}}{\Delta t_{c\xi}}\right)^\alpha\right]$$
$$S_{4\xi} = \frac{\sigma_{4\xi}}{J}\left[\frac{1}{\Delta t_{c\xi}}\left(1+\frac{\Delta t_{c\xi}}{\Delta t_{c\eta}}\right)^\alpha\right], \quad S_{4\eta} = \frac{\sigma_{4\eta}}{J}\left[\frac{1}{\Delta t_{c\eta}}\left(1+\frac{\Delta t_{c\eta}}{\Delta t_{c\xi}}\right)^\alpha\right] \tag{18}$$

Here, $\Delta t_{c\xi}$, $\Delta t_{c\eta}$ are timesteps corresponding to unit CFL limit for the inviscid one-dimensional problem in each direction:

$$\Delta t_{c\xi} = \frac{1}{|\tilde{G}_1| + a\sqrt{(\nabla\xi \cdot \nabla\xi)}}, \quad \Delta t_{c\eta} = \frac{1}{|\tilde{G}_2| + a\sqrt{(\nabla\eta \cdot \nabla\eta)}} \tag{19}$$

The choice of unit CFL scaling in the numerator of Eq. (19) ensures that the steady-state solution will be independent of the operational CFL limit used to compute local timesteps. If $\alpha = 1$, Eqs. (18) reduce to standard isotropic scaling. As mentioned above, this introduces excessive dissipation in the ξ direction in regions where the grid is stretched in the η direction. If $\alpha = 0$, the scaling becomes purely anisotropic. If the grid is very highly stretched in the η direction, such scaling may not provide enough dissipation in the ξ direction, resulting in reduced convergence rates. For intermediate values of α between 1/2 and 2/3, Martinelli,[15] Swanson and Turkel,[18] and Radespiel and Swanson[19] have shown good convergence rates for Euler and Navier-Stokes calculations on highly clustered grids.

Another scaling issue is important in the computation of viscous flows. All of the mean flow equations with the exception of the continuity equation contain physical dissipation terms. Near solid boundaries, the viscous fluxes in the momentum equations are quite large and are themselves adequate to provide smoothing. In these same regions, second and fourth derivatives of the transport variables can be quite large, leading to large values of artificial dissipation there. This well-recognized phenomenon (e.g., see Swanson and Turkel[18] and Davis et al.[20]) gives rise to very large nonphysical values of total dissipation in the near-wall region. Often some sort of geometric decay function is used to control the levels of artificial dissipation in these regions to reduce the magnitude of numerical to physical smoothing to acceptable levels. In the present work, the scaling functions in Eqs. (18) are multiplied by a normalized square of the local velocity $\tilde{V}^2/\tilde{V}_\infty^2$ for the momentum equations.

Following Jameson et al.,[1] the nonlinear weighting functions in Eqs. (18) are determined from

$$\sigma_{2\xi} = \kappa_2 \max(\nu_{\xi i+1,j}, \nu_{\xi i,j}, \nu_{\xi i-1,j}) \tag{20a}$$

$$\sigma_{4\xi} = -\max(0, \kappa_4 - \sigma_{2\xi}) \tag{20b}$$

where the monitoring parameters ν are normalized second derivatives of pressure

$$\nu_{\xi i,j} = \left| \frac{\bar{p}_{i+1,j} - 2\bar{p}_{i,j} + \bar{p}_{i-1,j}}{\bar{p}_{i+1,j} + 2\bar{p}_{i,j} + \bar{p}_{i-1,j}} \right| \tag{21}$$

and $\kappa_2 \cong 1/4$, $\kappa_4 \cong 1/50$. Expressions similar to Eqs. (20) and (21) are used in the η direction.

To examine the effects of the scalings given, a series of numerical experiments were conducted. The first experiment attempted to isolate the influence of eigenvalue scaling on accuracy and convergence. The subsonic cascade computation presented below was run using the following values of α in Eqs. (18): $\alpha = 1$ (standard isotropic scaling), $\alpha = 0$ (purely anisotropic scaling), and $\alpha = 2/3$ (intermediate scaling). As is shown in convergence history plots in the original version of this paper,[21] scaling the dissipation anisotropically does provide a slightly improved convergence rate for this case, as expected. In addition, purely anisotropic scaling provided a convergence rate somewhat superior to the weighted scaling ($\alpha = 2/3$). The influence of these scalings on accuracy was found to be negligible.

Further experiments sought to detect the influence of spurious artificial dissipation levels in near-wall boundaries, and to see how the proposed velocity scaling affects solution convergence and accuracy. First, developing turbulent flow over a flat plate was computed. When a standard value of $\kappa_4 = 0.02$ was used without velocity scaling, predicted law-of-the-wall velocity profiles were very poor, as shown in Fig. 1a. Note that κ_4 had to be reduced to 0.0005, a value too low to maintain numerical stability in most calculations, in order to bring the predicted profiles within good agreement of accepted laminar sublayer and overlap layer profiles. This is illustrated in Fig. 1b. In Fig. 1c, it is seen that using the standard value of $\kappa_4 = 0.02$ does not introduce enough excess artificial dissipation to corrupt the near-wall predictions, when the proposed velocity scaling is incorporated. The convergence histories for all three cases compared very closely, but law-of-the-wall predictions were seen to be much improved by incorporating velocity scaling.

Another experiment was carried out using the subsonic cascade case presented below. The calculation was run using $\kappa_4 = 0.02$, both with and without velocity scaling. When velocity scaling was not used, and the ratio of artificial to physical dissipation terms in Eq. (16) was compared, it was found that for this test case, at convergence, artificial dissipation levels were as high as 10 times the physical dissipation terms at the first several grid points adjacent to the wall! By incorporating the velocity scaling exactly as proposed above, it was possible to reduce the artificial to physical dissipation ratio to less than 0.01 in the near-wall region, except in the immediate vicinity of the leading and trailing edges. The convergence rates for the two cases compared very closely, but as shown in the original version of this paper,[21] the converged blade skin friction predictions showed significant discrepancy. It is clear from the foregoing examples that unnecessary levels of artificial dissipation in boundary layers can affect solution accuracy in practical application. Both eigenvalue scaling (with $\alpha = 2/3$) and local velocity scaling were used in all computations that follow.

Boundary and Initial Conditions

Along blade surfaces the no-slip condition is imposed on the velocities, pressure is extrapolated from adjacent grid points, and density is computed based on specified wall temperature or heat transfer rate. At the inlet, total pressure and total temperature are specified. For subsonic inflow, either inlet flow angle or pitchwise velocity are specified, and the R^- characteristic is extrapolated along η = constant grid lines from the interior of the computational domain. At subsonic outflow boundaries, static pressure is specified and velocity

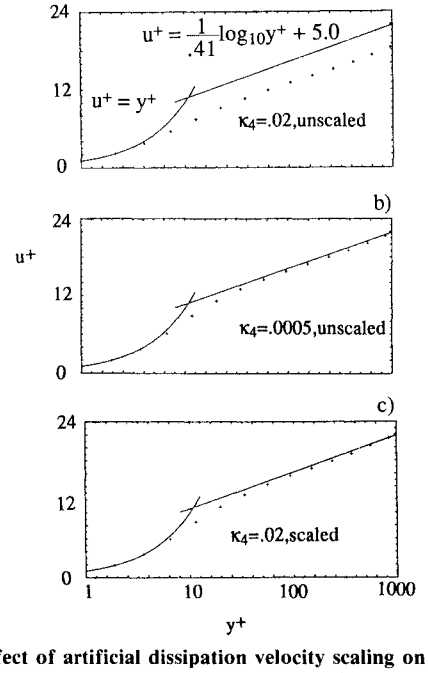

Fig. 1 Effect of artificial dissipation velocity scaling on law-of-the-wall predictions: symbols = computation, solid lines = law-of-the-wall relations.

components and entropy are extrapolated along η = constant grid lines. Along periodic boundaries, cyclic information is used when discretizing derivatives in the η direction. Constant values of k and ϵ are imposed at the inflow boundary based on specified freestream turbulence intensity and length scale

$$T_{u\infty} = \frac{\sqrt{2/3\tilde{k}_\infty}}{\tilde{V}_\infty}, \qquad L_\infty = \frac{C_\mu \tilde{k}^{3/2}}{\tilde{\epsilon}} \tag{22}$$

Typically, the freestream length scale is set between 0.001 and 0.01 times the pitch of the blade passage. At the outflow boundary, values of k and ϵ are extrapolated along η = const grid lines from the interior of the computational domain. Turbulent kinetic energy and isotropic dissipation rate are set to zero along solid boundaries.

Results and Discussion

Computational Considerations

The code has been validated for laminar and turbulent flat plate boundary-layer flows, where nearly exact agreement with theory and experiment were obtained. In addition, it has been applied to laminar and turbulent flows over a circular arc bump in a channel. In turbulent cases, the wall was heated and an algebraic eddy viscosity model was employed. These two model problems had been computed by Chima and Johnson[22] and Davis et al.,[20] respectively. The present method yielded nearly exact agreement with these two sets of results.

For turbulent flow calculations, the highly vectorized code executes at 2.8×10^{-5} CPU s/(gridpoint*iteration) on the Cray Y-MP 8/32 at the Pittsburgh Supercomputer Center. When an algebraic eddy viscosity model is used, the execution rate is 1.7×10^{-5} CPU s/(gridpoint*iteration). Experience with the code has shown that when the same grid is used, mean density residual converges slightly more slowly when using the k-ϵ model than when using the algebraic model, so the total overhead associated with using the k-ϵ model is less than a factor of 2.0.

To illustrate these considerations, convergence histories are presented for the prediction of developing turbulent flow over a flat plate. Both the algebraic eddy viscosity model developed by Baldwin and Lomax[23] and the present two-equation model were used. Both cases converged very slowly due to the extremely high aspect ratio of the grid (1.2×10^4 at the trailing edge of the plate). The convergence histories for the computations are shown in Fig. 2. Note that the convergence rates are similar. This illustrates that it is primarily hyperbolic and parbolic stability constraints associated with grid clustering, and not the stiffness associated with large source terms in the turbulence transport equations, that give rise to the slower convergence rates that occur when explicit schemes are used to compute turbulent flows on highly stretched meshes.

DFVLR PAV-1.5 Supersonic Compressor Cascade

The first cascade to be investigated is the PAV-1.5 supersonic compressor cascade tested at DFVLR by Schreiber.[24] The precompression blading was designed especially to investigate shock boundary-layer interaction with separation. At the test freestream Mach number, a standoff leading-edge shock forms, which gives rise to a separated shock boundary-layer interaction aft of midchord on the suction surface of the adjacent lower passage. Though the measured absolute inlet Mach number was supersonic, the blade row stagger angle was high, so the axial component of the inlet velocity was subsonic. This gives rise to the "unique incidence" condition wherein there exists a fixed relationship between inlet Mach number and inlet flow angle. Beyond a critical Mach number this condition exists and inlet conditions become independent of back pressure. This phenomena, as well as the complex wave interaction field within the passage and shock boundary-layer interaction, provide a challenge for both the numerical scheme and the turbulence model.

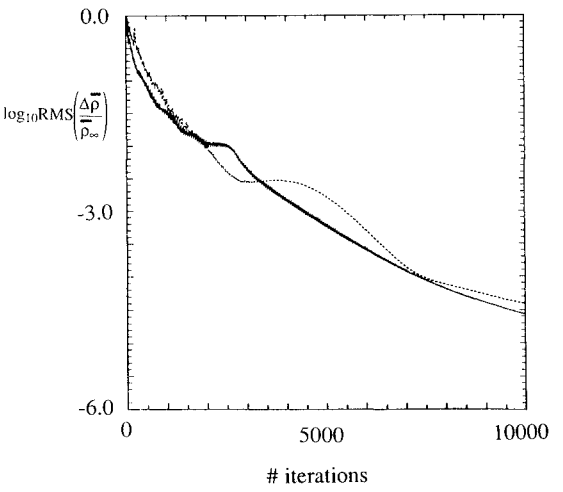

Fig. 2 Convergence history for turbulent flat plate boundary-layer calculations: solid line = Baldwin and Lomax,[23] dashed line = k-ϵ.

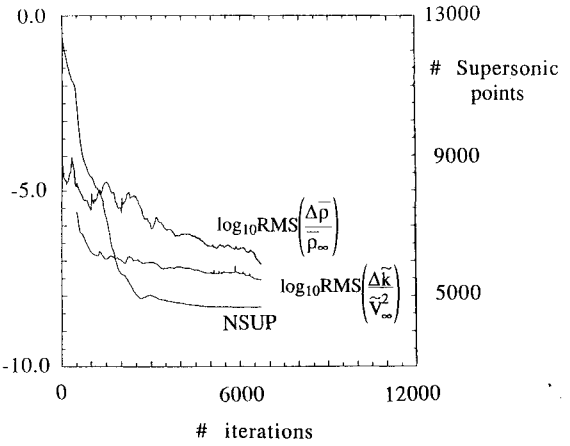

Fig. 3 Convergence history for PAV-1.5 cascade computation.

The computed case was experimentally tested in air at an inlet Mach number of 1.53 and a maximum attainable static pressure ratio of 2.13. The measured axial velocity density ratio (AVDR) of 1.02 indicates that the flow was close to two-dimensional. The Reynolds number based on chord was 2.7×10^6. The inlet turbulence intensity was measured, using a Laser-two-focus (L2F) velocimeter, to be no more than 1%, which is the value used in the computations. As previously mentioned, the inlet Mach number is supersonic, but axial velocity at the inlet to the computational domain is subsonic, allowing left running characteristics to propagate out of the inlet plane. For this reason, subsonic inlet boundary conditions were specified: $p_0 = 101325$ N/m^2, $T_0 = 300$ K, $V_{\theta\infty} = 379.5$ m/s^2. At the subsonic exit plane, the back pressure, $p_e = 56500$ N/m^2, was specified corresponding to the experimentally measured pressure ratio of the cascade, $p_2/p_1 = 2.13$.

A 129×100 computational mesh was used for this calculation (grid generation details and diagram available in the original paper[21]). The blade normal grid spacing at the wall was prescribed as 0.000011 chord. This yielded values of $y^+ \leq 1$ at grid points adjacent to the walls. Except in the immediate vicinity of the leading and trailing edges, the suction and pressure surface boundary layers had at least 9 grid points with values of $y^+ \leq 20$.

The convergence for this calculation is shown in Fig. 3. It took approximately 6500 iterations for this calculation to converge within engineering accuracy as measured by the invariance of total number of supersonic gridpoints in the field. This corresponded to approximately 39 min of CPU time on the

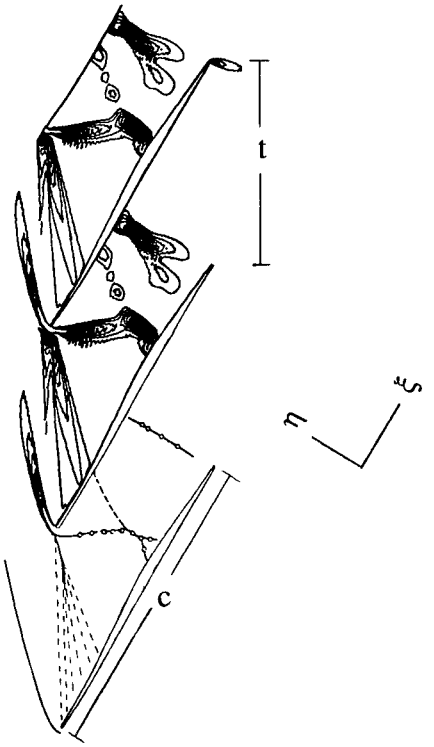

Fig. 4 Shock wave pattern for PAV-1.5 cascade, presented as divergence of velocity contours [−300 to −4800 × −500 (s^{-1})]. The top two passages show computed contours; the bottom passage is the shock wave pattern deduced from flow visualization and L2F measurements, reproduced from Schreiber.[24]

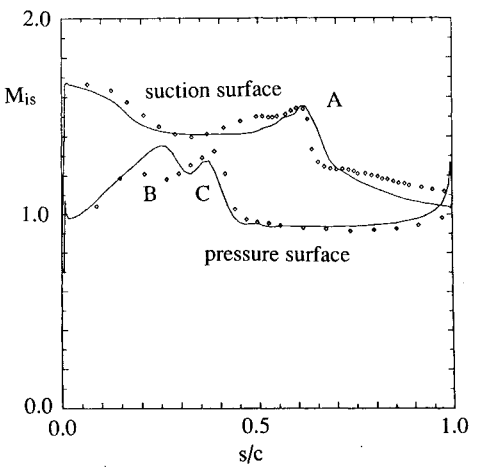

Fig. 5 Isentropic blade surface Mach numbers for PAV-1.5 cascade computation: calculated (solid line) and experimental values[24] (symbols).

Pittsburgh Cray. It was not possible to "cold start" the initialized flowfield at the specified pressure ratio, as the code became rapidly unstable when this was attempted. Rather, the back pressure had to be increased in a stepwise fashion with iteration to achieve the experimentally measured pressure ratio. (Notice the "jumps" in convergence history at iteration 500, 1000, 2000.)

In Fig. 4, a hand rendering of the shock wave pattern deduced from L2F measurements has been reproduced from Schreiber,[24] alongside the computed shock wave pattern presented as divergence of velocity contours. The key features of the flowfield are evident in this diagram, including the bow, lambda, and passage shocks. In both experiment and computation, the bow shock is seen to impinge on the suction surface boundary layer of the adjacent lower passage. This gives rise to a lambda shock structure, a rapid thickening and separation of the boundary layer, and a Mach reflection that impinges on the pressure surface of the same passage. The high pressure ratio operating condition of this test case gives rise to a normal passage shock that impinges upstream of midchord on the pressure surface. This feature is also evident in both experiment and computation. The computation also shows some evidence of an oblique trailing-edge shock, typical of supersonic compressor cascades at high operating pressure ratios.

In Fig. 5, the predicted isentropic blade surface Mach number is plotted against the experimental values. The calculation and experiment show fairly good agreement. The features labelled A, B, and C in Fig. 5 correspond to local compression regions, where the bow shock impinges on the suction surface, the Mach reflection impinges on the pressure surface, and the passage shock impinges on the pressure surface.

In Fig. 6, the computed total pressure ratio is compared with traverse probe measurements at an axial location 0.09 chord downstream of the cascade exit plane. The wake profile and loss distribution is reasonably well predicted, with the losses associated with the lambda shock system underpredicted. The wake centerline total pressure ratio is predicted reasonably well, considering the difficulty in measurement at this location. It is noted that the results presented for this cascade are not fully grid independent. Modifications in the pitchwise grid clustering near midpassage gave rise to as much as a 2% chord difference in the impingement location of the bow shock on the suction surface, and a 5% chord difference

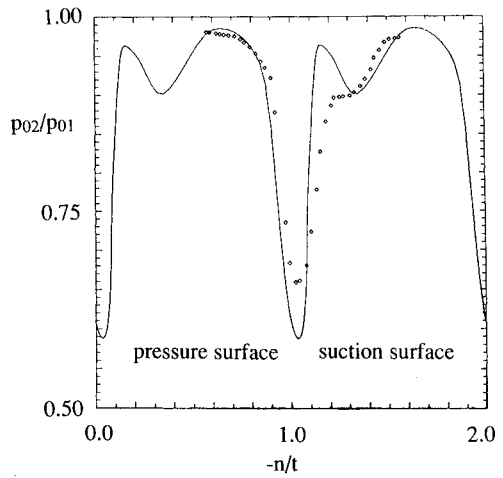

Fig. 6 Total pressure ratio profile 0.09 chord downstream of trailing edge for PAV-1.5 cascade computation: calculated (solid line) and experimental values[24] (symbols).

Table 1 Comparison of cascade flow parameters for computed cases

Flowfield parameter	Measured	Computed	Difference
	PAV-1.5		
C_L[a]	≅ 0.43	0.38	≅ 12%
ω[b]	0.144	0.149	3.4%
β_1	− 1.8 deg	− 1.3 deg	0.5 deg
β_2	2.7 deg	3.1 deg	0.4 deg
$s/c_{sep_{ss}}$	0.63	0.67	6.3%
$s/c_{sep_{ps}}$	≅ 0.40	0.40	≅ 0.0
AVDR	1.02	1	NA
	ARL DCA		
C_L[a]	0.82	0.88	7%
ω[b]	0.094	0.111	18%
β_1	− 1.5 deg	prescribed	NA
β_2	14.1 deg	13.0 deg	1.1 deg
$s/c_{sep_{ss}}$	0.45	varies	NA
$s/c_{sep_{ps}}$	none	none	NA
AVDR	0.97–1.03	1	NA

[a]Lift coefficient computed from C_L = (lift per unit span) ⊥ $V_m/0.5\rho_m V_m^2$.
[b]Pressure loss coefficients computed from $\omega = (p_{0\infty} - p_0)/(0.5\rho_\infty V_\infty^2)$ for ARL and $\omega = (p_{0\infty} - p_0)/(p_{0\infty} - p_\infty)$ for PAV.

in the location of the passage shock. The loss distribution aft of the blade was hardly affected, but the blade surface Mach number distributions varied somewhat. Predicted and measured performance parameters for this cascade, operating at the given conditions, are presented in Table 1.

Schreiber[24] provided measured loss coefficients at maximum attainable cascade pressure ratio for a number of operating inlet Mach numbers. For comparison, the code was run at two operating points within the envelope of the experimental tests. Figure 7 shows computed total pressure loss coefficients at all three operating points computed, along with the envelope of experimental values. It is noted that Schreiber[24] attributes the scatter in measured loss coefficient to variations in experimental axial velocity density ratio.

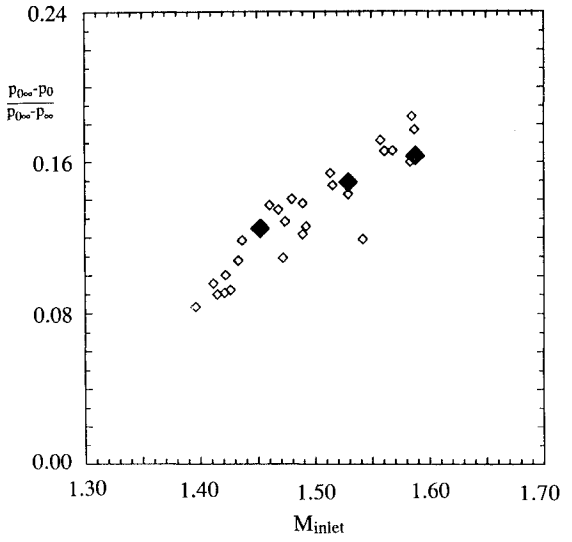

Fig. 7 Total pressure loss coefficients at several cascade operating points: experiment[24] (open symbols) and computation (solid symbols).

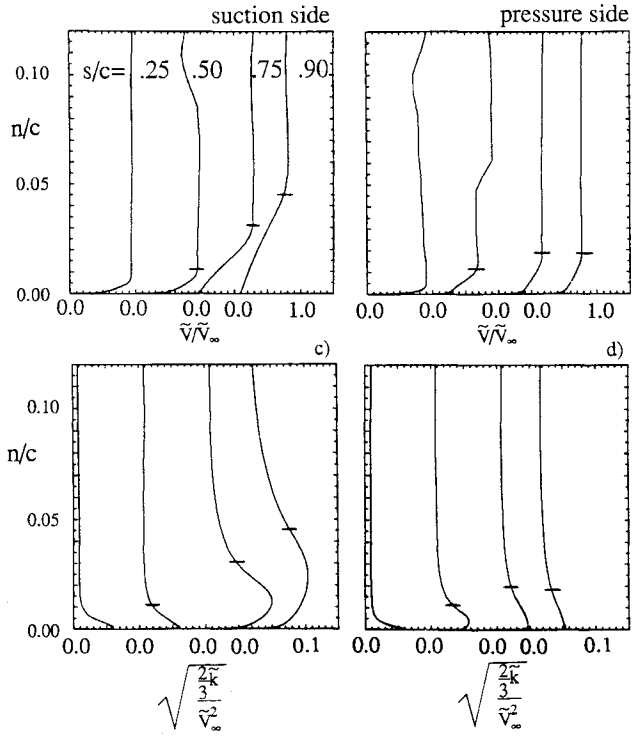

Fig. 8 Computed blade boundary-layer velocity and turbulent kinetic energy profiles at several chordwise locations for PAV-1.5 cascade; hash marks show estimated experimental boundary-layer thicknesses.[24]

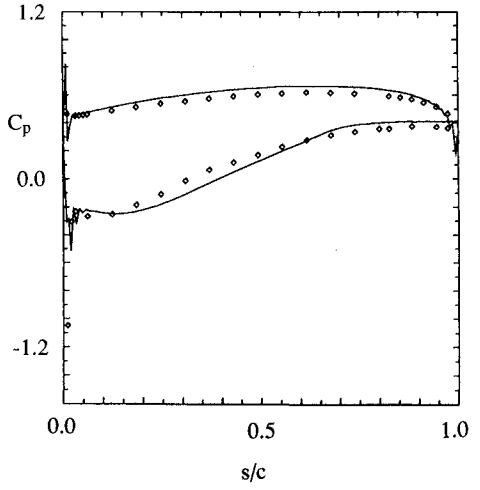

Fig. 9 Pressure coefficient for ARL DCA cascade computation: calculated (solid line) and experimental values[25] (symbols).

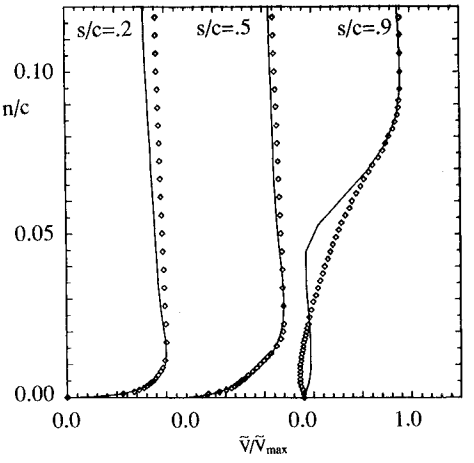

Fig. 10 Boundary-layer profiles at three chord locations along the suction surface for the ARL DCA cascade computation: calculated (solid line) and experimental values[25] (symbols).

Predicted near blade boundary-layer total velocity and turbulent kinetic energy profiles are presented in Fig. 8. The predicted boundary-layer thicknesses compare well with those estimated by Schreiber.[24] The simulation provides a representation of near-wall physics that were not measured.

Applied Research Laboratory Double Circular Arc Subsonic Compressor Cascade

The second cascade flow to be computed is the Applied Research Laboratory (ARL) double circular arc (DCA) cascade tested at Penn State by Zierke and Deutch.[25] The computed case was tested at a negative incidence of 1.5 deg. The working fluid was air at standard atmosphere with an inlet velocity of 32.9 m/s (inlet Mach number = 0.1). The Reynolds number based on chord was 5.0×10^5. The measured axial velocity ratio was measured to be between 0.97 and 1.03, indicating that the flow was close to two-dimensional. It is noted that the present solution method, which incorporates a compressible formulation of the Navier-Stokes equations, is not well-suited to this low Mach number flow. Inlet turbulence intensity was specified at 2% so as to match measured local freestream intensity at 20% chord on the suction surface.

A 129×85 computational mesh was used for this calculation (grid generation details and diagram available in the original paper[21]). Grid spacing in the blade normal direction was set to 0.000023 chord on the blade surfaces. This yielded values of $y^+ \leq 1$ at grid points adjacent to the walls. Except in

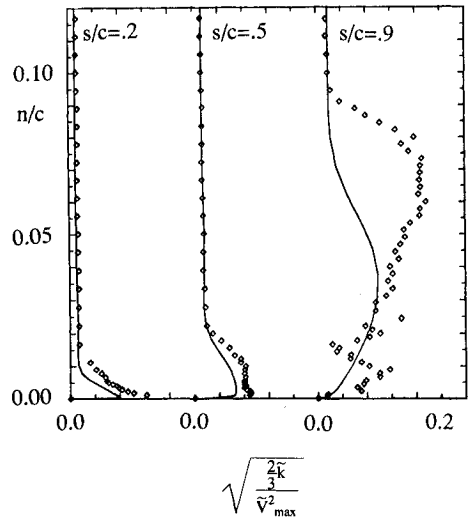

Fig. 11 Local turbulence intensity profiles at three chord locations along the suction surface for the ARL DCA cascade computation: calculated (solid line) and experimental values[25] (symbols).

the immediate vicinity of the leading and trailing edges, the suction and pressure surface boundary layers had at least 11 grid points with values of $y^+ \leq 20$.

It was only possible to obtain a steady solution when a coarse "preliminary" grid was used for this case. These coarse grid calculations overpredicted skin friction along the entire length of the suction surface, so the flow remained attached and a steady-state solution was achieved. The more refined grid adequately resolved both inner layer and core flow regions, yielding more accurate skin friction and boundary-layer profiles. However, because both calculation and experiment show regions of mean flow reversal near the trailing edge, it was not possible to obtain a steady solution.

It took approximately 7000 iterations for this calculation to acquire a 4.5 order of magnitude drop in the rms density residual. (Convergence history is available in the original paper.[21]) This corresponds to approximately 36 min of CPU time on the Cray Y-MP. Beyond this point, however, the residual changes begin to increase and then level off in a quasiperiodic fashion. This is attributed to unsteady shedding of vorticity from the aft portion of the suction surface.

Despite the lack of a steady-state solution, the flow along the blade remained relatively unchanged after 7000 iterations, except for quasiperiodic shifts in the boundary-layer velocity and turbulence intensity profiles. The measured flow also showed a small region of mean backflow near the trailing edge of the blade,[25] and for that reason was also probably unsteady. In Fig. 9, comparison is made betwen computed blade surface pressure coefficient and measured values. Agreement is good along both blade surfaces. The oscillations in the pressure distributions near the leading and trailing edges in Fig. 9 are caused by the velocity scaling of the artificial dissipation. The H-grid used gives rise to highly skewed regions near the relatively blunt leading and trailing edges of this configuraiton, causing the velocity scaling presented "as is" to give rise to these oscillations. Though the cascade flow solution is not significantly affected, it may be worth investigating improved scaling.

In Fig. 10, the predicted boundary-layer profiles at three chordwise locations on the suction surface are plotted with those measured by laser doppler velocimeter. Agreement is excellent at 20 and 50% chord, but not very good at 90% chord. The relatively poor predictions at 90% chord are probably attributable to flowfield unsteadiness in this region. Local turbulence intensity profiles are presented for three chordwise locations on the suction surface in Fig. 11. As above, agreement between calculation and experiment is good at the first two stations, though not very good in the aft portion of the blade. Predicted and measured performance parameters for this cascade are also presented in Table 1.

Conclusions

A Navier-Stokes procedure has been developed and applied to a supersonic and low subsonic compressor cascade. A compressible low Reynolds number form of the k-ϵ turbulence model was used. The following was concluded:

1) A fully explicit treatment of the turbulence transport equations is possible. The computational overhead associated with this treatment is reasonable.

2) It is crucial to incorporate local timestep constraints based on a stability analysis of the full viscous mean flow equations if the k-ϵ model is used for an H-grid cascade calculation.

3) The highly stretched grids needed to resolve near-wall physics warrant eigenvalue and local velocity scaling of artificial dissipation terms to improve accuracy and convergence rates.

4) Flowfield predictions were found to be good for a supersonic cascade and fair for a low subsonic cascade.

5) Overall cascade performance parameters were well predicted for the supersonic cascade but, due to flowfield unsteadiness, not well predicted for the low subsonic cascade.

Acknowledgments

The first author was suppported by a U.S. Army Research Office fellowship, through Grant DAAL03-86-G-0044, monitored by T. L. Doligalski. The authors wish to acknowledge the National Science Foundation supported Pittsburgh Supercomputer Center (Grants MSM860009P and CBT90015P) for providing supercomputing resources. In addition, the following were helpful in providing assistance and suggestions in the course of carrying out this work: R. Chima, S. Connell, G. Dulikravich, H. Schreiber, and the journal associate editor and reviewers.

References

[1]Jameson, A., Schmidt, W., and Turkel, E., "Numerical Solutions of the Euler Equations by Finite Volume Methods Using Runge-Kutta Time-Stepping Schemes," AIAA Paper 81-1259, June 1985.

[2]Speziale, C. G., "Discussion of Turbulence Modelling: Past and Future," ICASE Rept. 89-58, July 1989.

[3]Lakshminarayana, B., "Turbulence Modelling for Complex Flows," AIAA Paper 85-1652, July 1985.

[4]Kirtley, K., and Lakshminarayana, B., "Computation of Internal Incompressible Separated Flows Using a Space Marching Technique," AIAA Paper 85-1624, July 1985.

[5]Degrez, G., and VanDromme, D., "Implicit Navier-Stokes Calculations of Transonic Shock/Turbulent Boundary-Layer Interactions," *Turbulent Shear-Layer/Shock-Wave Interactions*, edited by J. Delery, IUTAM Symposium, Palaiseau, France, Springer-Verlag, 1985.

[6]Liu, J. S., "Navier-Stokes Cascade Analysis With the k-ϵ Turbulence Model," Ph.D. Dissertation, MAE, Case Western Reserve Univ., Cleveland, OH, 1987.

[7]Grasso, F., and Speziale, C. G., "Supersonic Flow Computations by Two-Equation Turbulence Modelling," AIAA Paper 89-1951, June 1989.

[8]Eliasson, P., "Solutions to the Navier-Stokes Equations Using a k-ϵ Turbulence Model," Flygtekniska Forsoksanstalten TN-1988-19, Stockholm, Sweden, 1988.

[9]Holmes, D. G., and Connell, S. D., "Solution of the 2D Navier-Stokes Equations on Unstructured Adaptive Grids," AIAA Paper 89-1932, June 1989.

[10]Favre, A., "Equations des Gaz Turbulents Compressibles: 1, Formes Generales," *Journal de Mechanique*, Vol. 4, 1965.

[11]Jones, W. P., "Models for Turbulent Flows with Variable Density and Combustion," *Prediction Methods for Turbulent Flows*, edited by W. Kollmann, Hemisphere, London, 1980, pp. 380–420.

[12]Chien, K., "Predictions of Channel and Boundary-Layer Flows with a Low-Reynolds-Number Turbulence Model," *AIAA Journal*, Vol. 20, No. 1, 1982, pp. 33–38.

[13]Coakley, T. J., "Turbulence Modelling Methods for the Com-

pressible Navier-Stokes Equations," AIAA Paper 83-1693, July 1983.
[14]Hobson, G. V., private communication, 1989.
[15]Martinelli, L., "Calculation of VIscous Flows with Multigrid Methods," Ph.D. Dissertation, MAE Dept., Princeton Univ., Princeton, NJ, 1987.
[16]Pulliam, T. H., "Artificial Dissipation Models for the Euler Equations" *AIAA Journal,* Vol. 24, No. 12, 1986, pp. 1931-1940.
[17]Caughey, D. A., and Turkel, E., "Effects of Numerical Dissipation on Finite Volume Solutions of Compressible Flow Problems," AIAA Paper 88-0621, Jan. 1988.
[18]Swanson, R., and Turkel, E., "Artificial Dissipation and Central Difference Schemes for the Euler and Navier-Stokes Equations," NASA CR-178296, April 1987.
[19]Radespiel, R., and Swanson, R., "An Investigation of Cell Centered and Cell Vertex Schemes for the Navier Stokes Equations," AIAA Paper 89-0548, Jan. 1989.
[20]Davis, R. L., Ni, R., and Carter, J. E., "Cascade Viscous Flow Analysis Using the Navier-Stokes Equations," AIAA Paper 86-0033, Jan. 1986.
[21]Kunz, R. F., and Lakshminarayana, B., "Computation of Supersonic and Low Subsonic Cascade Flows Using an Explicit Navier-Stokes Technique and the k-ϵ Turbulence Model," NASA CP-10045, April 1990.
[22]Chima, R. V., and Johnson, G. M., "Efficient Solutions of the Euler and Navier-Stokes Equations With a Vectorized Multiple-Grid Algorithm," *AIAA Journal,* Vol. 23, No. 1, 1985, pp. 22-32.
[23]Baldwin, B. S., and Lomax, H., "Thin Layer Approximation and Algebraic Model for Separated Turbulent Flows," AIAA Paper 78-257, Jan. 1978.
[24]Schreiber, H. A., "Experimental Investigations on Shock Losses of Transonic and Supersonic Compressor Cascades," AGARD CP-401, Paper 11, March 1987.
[25]Zierke, W. C., anhd Deutsch, S., "The Measurement of Boundary Layers on a Compressor Blade in Cascade: Part 4—Flow Fields for Incidence Angles of − 1.5 and − 8.5 Degrees," American Society of Mechanical Engineers, Paper 89-GT-72, June 1989.